

Low-Complexity Adaptive Sonar Imaging

Jo Inge Buskenes, Roy Edgar Hansen, *Member, IEEE*, and Andreas Austeng

Abstract—We have studied the low-complexity adaptive (LCA) beamformer in active sonar imaging. LCA can be viewed as either a simplification of the minimum variance distortionless response (MVDR) beamformer, or as an adaptive extension to the delay-and-sum (DAS) beamformer. While both LCA and MVDR attempt to minimize the power of noise and interference in the image, MVDR achieves this by computing optimal array weights from the spatial statistics of the wavefield, while LCA selects the best performing weights out of a predefined set. To build confidence in the LCA method, we show that a robust MVDR implementation typically creates weight sets with shapes spanning between a rectangular and Hamming window function. We let LCA select from a set of Kaiser windows with responses in this span, and add some steered variations of each. We limit the steering to roughly half the -3-dB width of the window's amplitude response. Using experimental data from the Kongsberg Maritime HISAS1030 sonar we find that LCA and MVDR produce nearly identical images of large scenes, both being superior to DAS. On point targets LCA is able to double the resolution compared to DAS, or provide half that of MVDR. This performance is achieved with a total of six windows: the rectangular window and the Kaiser window with $\beta = 5$, in an unsteered version, and versions that are left and right steered to the steering limit. Slightly smoother images are produced if the window count is increased to 15, but past this we observe minimal difference. Finally, we show that LCA works just as well if Kaiser windows are substituted with trigonometric ones. All our observations and experiences point to LCA being very easy to understand and manage. It simply works, and is surprisingly insensitive to the exact type of window function, steering amount, or number of windows. It can be efficiently implemented on parallel hardware, and handles any scene without the need for parameter adjustments.

Preferred: Beamforming, adaptive beamforming, MVDR, LCA, sonar, active, complexity.

From taxonomy v101: Sonar, adaptive filters, phased arrays, active filters, spatial filters, computational complexity

I. INTRODUCTION

THE best sonar in existence is perhaps found in nature. Bats, for instance, use a high-frequency sonar to detect, identify, and track prey with amazing precision in caves among a myriad of other bats. No man-made sonar can currently match this feat, much due to the challenge of processing and adapting to such a complex environment fast enough. This is why man-made sonars have little to no adaptivity on transmit. However, several methods have been investigated to adaptively process the received acoustic data. Perhaps the best studied method for

Manuscript received October 17, 2015; revised March 2, 2016; accepted May 2, 2016.

Associate Editor: D. Simons.

J. I. Buskenes and A. Austeng are with the Department of Informatics, University of Oslo, Oslo 0316, Norway (e-mail: joibu@ifi.uio.no; andrea@ifi.uio.no).

R. E. Hansen is with the Department of Informatics, University of Oslo, Oslo 0316, Norway, and also with the Norwegian Defense Research Establishment (FFI), Kjeller 2027, Norway (e-mail: rhn@ifi.uio.no; roy-edgar.hansen@ffi.no).

This paper has supplementary downloadable materials available at <http://ieeexplore.ieee.org>, provided by the author. The material contains two videos and the source code for determining steering boundaries for LCA's windows. Contact J. I. Buskenes at joibu@ifi.uio.no for further questions about this work.

Digital Object Identifier 10.1109/JOE.2016.2565038

reconstructing a sonar image out of such data is the minimum variance distortionless response (MVDR) beamformer [1]. It adapts the sonar array's spatial response to minimize the influence of noise and interference in the final image.

In many cases, MVDR can improve the contrast and resolution of active sonar images compared to conventional static methods [2]–[4]. However, while the computational complexity of conventional beamformers is linear with the number of channels $O(M)$, MVDR is at $O(M^3)$. This is because MVDR relies on estimating and inverting a covariance matrix. The estimation step dominates the computation in sonar systems with fewer than 32 channels, but here the computational complexity can be reduced and the implementation accelerated significantly using graphics computing units (GPUs) [5]. For larger systems the inversion step dominates. This can be dealt with by approximating the full covariance matrix with a small one using space reduction techniques such as beamspace processing [6], or the closely related principal component analysis (PCA) [7]. Another alternative is to assume spatial stationarity to form more easily invertible Toeplitz matrices [8]. However, the mentioned methods are still relatively slow compared to DAS.

A much faster and simpler alternative to MVDR is the low-complexity adaptive (LCA) beamformer. Based on an idea of Vignon and Burcher [9], the method was first introduced by Synnevåg *et al.* in clinical medical ultrasound imaging [10], who demonstrated its ability to obtain very similar image quality to MVDR in systems with focused transmit beams. LCA applies a set of predefined and static windows, or apodization weights, and selects the one offering the best noise suppression. It relies on the same optimization criterion as MVDR, thus may be considered a version of MVDR with a discrete and static window solution space. Alternatively, it may be viewed as a multiapodization technique. One such method is described by Stankwitz *et al.* in radar imaging [11], where the best out of two or three windows is selected. However, LCA differs in that it typically selects from a larger pool of windows and allows phase-steered variations of them. Phase-shifting the windows has the effect of slightly adjusting the angle the array is steered toward. This gives LCA an adaptive freedom that lies somewhere in between that of traditional multiapodization techniques and MVDR. How similarly LCA performs compared to MVDR depends on how well the predefined windows represent the constrained solution space of MVDR.

Synnevåg *et al.* suggested using a window set comprising rectangular, Kaiser (or Kaiser-Harris), and inverted Kaiser functions. In total, they let LCA choose from 12 unique windows, six of which were phase-shifted versions of a fairly wide Kaiser window, and one was rectangular. Synnevåg *et al.*'s composition of windows was motivated by the desire to use wide windows with maximum sidelobe suppression near the receiver, and narrow windows at greater depths for maximum sensitivity and

96 depth penetration. While they achieved good results, it was not
 97 made clear how many windows LCA needs, or how they ideally
 98 should be steered. Also, it is not apparent how LCA performs
 99 in sonar systems where the transmit beam is unfocused.

100 In this study, we expand our previous work of applying LCA
 101 to active sonar imaging [12]. We use variations of the parametric
 102 Kaiser window, but also compare it to the trigonometric win-
 103 dow function. We extend Synnevåg *et al.*'s work by steering all
 104 our windows and not just some, and demonstrate how LCA's
 105 performance is affected by the type and number of windows
 106 included. Our results are obtained using experimental data from
 107 the 32-element Kongsberg Maritime HISAS1030 sonar, which
 108 operates at 100 kHz with an -3 -dB element opening angle of
 109 23° . Although this system was designed as a synthetic aper-
 110 ture sonar (SAS) where an image is synthesized from several
 111 pings of data, we will only create images out of single pings
 112 (sectorscan imaging) in this study.

113 Our results show that when MVDR is robustified to work
 114 in active sonar imaging, it computes weights with spatial am-
 115 plitude responses that tend to be symmetric and steered within
 116 a fraction of their -3 -dB widths. When letting LCA choose
 117 from Kaiser windows with similar responses, we obtain images
 118 with improved noise suppression and resolution. The resolution
 119 gain is made predictable by limiting the maximum steering to
 120 a fraction of the -3 -dB width of each window's spatial ampli-
 121 tude response. Overall, LCA produces images that are similar
 122 to MVDR, but with a resolution in between that of DAS and
 123 MVDR. LCA is also inherently robust, easy to implement, and
 124 fairly easy to understand.

125 This paper is outlined as follows. In Section II, we offer a gentle
 126 introduction to beamforming. Then, we move on to adaptive
 127 beamforming and describe the MVDR and LCA methods in
 128 Sections III and IV, respectively. We use LCA with the Kaiser
 129 window which we describe in Section IV-A, we explain how
 130 we steer it in Section IV-B, and we discuss by how much in
 131 Section IV-C. Finally, we add some remarks on using the
 132 trigonometric window instead of Kaiser in Section IV-D and
 133 of sampling considerations in Section IV-E. Results and dis-
 134 cussion are provided in Section V, where we study MVDR's
 135 windows to find suitable LCA ones in Section V-A, assess the
 136 range of window types and steering in Section V-B, determine
 137 the number of windows needed in Section V-C. We add a
 138 note on computational complexity in Section V-E. Finally,
 139 Section VI provides a conclusion.

II. RECEIVE BEAMFORMING

140 A sonar image is formed by estimating source locations and
 141 amplitudes. For this purpose, a spatial bandpass filter is applied
 142 to the backscattered wavefield data. The filter is called an array
 143 processor or a receive beamformer. The basic principle is to
 144 apply delay and weights to the sensor channels before summing
 145 them up, chosen such that signals from the location of interest
 146 are summed coherently, while other sources sum incoherently.

147 Assume that the wavefield has been sampled by an M element
 148 uniform linear array, and that the signal signature has been
 149 removed by a matched filter. Let $x_m[\theta, n]$ be the delayed data

150 from the m th channel, where θ and n are the azimuth angle and
 151 the range sample of the focus point, respectively. Each angle θ
 152 will be processed independently, so to simplify notation we will
 153 assume the dependence on θ to be implicit from now on.
 154

155 The output $z[n]$ of a beamformer is defined as the weighted
 156 sum of all the delayed data samples

$$z[n] = \mathbf{w}^H[n] \mathbf{x}[n] = \begin{bmatrix} w_0[n] \\ w_1[n] \\ \vdots \\ w_{M-1}[n] \end{bmatrix}^H \begin{bmatrix} x_0[n] \\ x_1[n] \\ \vdots \\ x_{M-1}[n] \end{bmatrix} \quad (1)$$

157 where w_m is the weight factor assigned to channel m . A weight
 158 set is commonly called a window, an apodization, or a taper
 159 function. When the window is real, its response is symmetric.
 160 Applying a real window that trails off toward the edges creates a
 161 response with lower sidelobe levels and wider mainlobe, which
 162 translates into improved noise suppression at the cost of reduced
 163 resolution, respectively [13].
 164

Conventional beamformers all have static and usually real
 165 weights. The reference method is the delay-and-sum (DAS)
 166 beamformer, also known as the backprojection algorithm. It de-
 167 lays each pixel into focus, then applies a suitable window, and
 168 finally sums the data. The virtue of DAS is its simplicity, robust-
 169 ness to parameter errors, linear processing of the image, and the
 170 ease with which it can be implemented in parallel hardware.
 171

Adaptive beamformers are dynamic and seek to adjust the
 172 array response to better fit the incoming wavefield. This may
 173 be achieved by allowing either the weights or delays, or both,
 174 to change. Here the weights are usually complex, which al-
 175 lows asymmetric responses. One of the most extensively stud-
 176 ied adaptive methods is the minimum variance distortionless
 177 response (MVDR) beamformer.

III. MINIMUM VARIANCE DISTORTIONLESS RESPONSE

MVDR seeks to minimize the power of noise and interference
 178 in the output of the beamformer, under the constraint of unity
 179 gain in some desired direction ϕ [1]. With the assumption of zero
 180 mean data, this takes the form of minimizing output variance
 181

$$\underset{\mathbf{w}[n]}{\operatorname{argmin}} E\{|z[n]|^2\} = \underset{\mathbf{w}[n]}{\operatorname{argmin}} \mathbf{w}[n] \mathbf{R}[n] \mathbf{w}^H[n] \\ \text{subject to } \mathbf{w}^H[n] \mathbf{a}_\phi = 1. \quad (2)$$

Here \mathbf{a}_ϕ is a steering vector for an azimuthal steering angle ϕ ,
 183 $E\{\cdot\}$ is the expectation operator, and $\mathbf{R}[n] = E\{\mathbf{x}[n] \mathbf{x}^H[n]\}$
 184 is the spatial covariance matrix for the full array. This is a convex
 185 optimization problem with the unique solution
 186

$$\mathbf{w}[n] = \frac{\mathbf{R}^{-1}[n] \mathbf{a}_\phi}{\mathbf{a}_\phi^T \mathbf{R}^{-1}[n] \mathbf{a}_\phi}. \quad (3)$$

The problem lies in estimating and inverting the spatial covari-
 187 ance matrix. We have described the exact steps in [5]: To avoid
 188 signal cancellation, we apply spatial averaging by computing a
 189 mean covariance matrix from a set of subarrays with length L
 190 [14]. For true speckle statistics, we perform temporal averaging
 191

192 over $N_k = 2K + 1$ temporal samples [15], and to improve ro-
 193 bustness to parameter errors, we add ϵ percent of the total output
 194 power to the matrix's diagonal [16], [17]. These steps are also
 195 needed to ensure that the covariance matrix is numerically well
 196 conditioned and hence invertible.

197 IV. LOW-COMPLEXITY ADAPTIVE

198 A much less complex alternative to MVDR is the LCA beam-
 199 former. It iterates through a set of P windows and selects win-
 200 dow p that best fulfills the minimum variance criterion

$$\begin{aligned} \operatorname{argmin}_p E\{|z_p[n]|^2\} &= \operatorname{argmin}_p E\left\{\left|\mathbf{w}_p^H \mathbf{x}[n]\right|^2\right\} \\ \text{subject to } \mathbf{w}^H \mathbf{a}_\phi &= 1. \end{aligned} \quad (4)$$

201 Note how closely LCA is related to the MVDR definition in
 202 (2). The optimization criterion and constraint is the same, but
 203 LCA has a finite and discrete solution space for the weights. As
 204 will be demonstrated in Section V-A, LCA performs similarly
 205 to MVDR because a robustified MVDR implementation seems
 206 to be constrained to window functions similar to the ones we let
 207 LCA choose from.

208 In practice, we estimate the beamformer output power by
 209 computing a sample power average s_z^2

$$E\{|z[n]|^2\} \approx s_z^2 = \frac{1}{N_k} \sum_{n=t-K}^{n+K} |z[n]|^2$$

210 which computes the sample power average over $N_k = 2K + 1$
 211 temporal samples. This is the same temporal averaging method
 212 we use for MVDR. In our case, the bandwidth of our matched
 213 filtered signal is just a few samples long, hence $K = 1$ will be
 214 used for both MVDR and LCA throughout this work.

215 If pixels are correlated laterally, we can include a weighted
 216 combination of these to improve the variance estimation

$$s_z^2 = \frac{1}{N_x N_k} \sum_{x'=-X}^{x+X} \sum_{n'=-K}^{n+K} \omega[x', n'] |z[x', n']|^2 \quad (5)$$

217 where $N_x = 2X + 1$ is the number of azimuth lines to aver-
 218 age over, and $\omega[x', n']$ is a normalized 2-D weight function.
 219 Since we oversample slightly laterally when we delay each pixel
 220 (see Section IV-E), we think the lateral correlation to be suf-
 221 ficient to benefit from this. However, we observe no visual
 222 improvement from applying this technique, and decide not to
 223 use it.

224 A. Window Function: Kaiser

225 As will be demonstrated in the upcoming sections, the LCA
 226 beamformer works very well with windows generated from the
 227 Kaiser-Bessel function. We will express it in a vector form as

$$\mathbf{f}_\beta = \begin{bmatrix} f_0(\beta) \\ \vdots \\ f_{M-1}(\beta) \end{bmatrix} \quad (6)$$

where

$$f_m(\beta) = \frac{I_0\left(\pi\beta\sqrt{1-\left(\frac{2m}{M-1}-1\right)^2}\right)}{I_0(\pi\beta)} \quad (7)$$

and I_0 is the zeroth-order modified Bessel function of the first kind

$$I_0(x) = \sum_{a=0}^{\infty} \left[\frac{\left(\frac{x}{2}\right)^a}{a!} \right]^2. \quad (8)$$

The Kaiser-Bessel window is near optimal in the sense of having its peak energy concentration around $\theta = 0^\circ$, for a given space-bandwidth product related to the Kaiser parameter β as

$$\beta = \frac{TB}{2} \quad (9)$$

where T in our case is the spatial extent of the window and B is its bandwidth. Adjusting β changes the tradeoff between the mainlobe width and the sidelobe level. When $\beta = 0$, the window becomes rectangular, while at large values ($\beta > 5$), the window converges to a Gaussian, both in time and frequency. This class of windows is generally considered to be well suited for separating closely spaced sources with amplitudes of a high dynamic range [13]. They are easy to make, and they are optimal for any value of β .

243 B. Steering

Adding slightly steered versions of each window to the window database gives LCA greater flexibility in searching for an optimal window. A Kaiser window \mathbf{f}_β steered to the azimuth angle ϕ can be expressed as

$$\mathbf{w}_{\beta, \phi} = \frac{\mathbf{f}_\beta^H \operatorname{diag}(\mathbf{a}_\phi)}{\mathbf{f}_\beta^H \mathbf{a}_\phi} \quad (10)$$

where $\operatorname{diag}(\mathbf{a}_\phi)$ is a diagonal matrix constructed from the steering vector \mathbf{a}_ϕ

$$\mathbf{a}_\phi = \begin{bmatrix} 1 \\ e^{-j\frac{2\pi d}{\lambda} \sin(\phi)} \\ \vdots \\ e^{-j\frac{2\pi(M-1)d}{\lambda} \sin(\phi)} \end{bmatrix}. \quad (11)$$

Here d is the element spacing, λ is the wavelength, and ϕ is the steering amount. The normalization factor $\mathbf{f}_\beta^H \mathbf{a}_\phi$ is the reciprocal of the window's coherent gain. It ensures unit gain in the direction of interest as required by (4). Since the signal-to-noise ratio is constant for a specific window (the same β -value), this normalization also proportionally increases the incoherent noise gain.

The window database we will construct will contain N_β Kaiser windows with unique β -values, each being steered in N_ϕ different directions. This gives us $N_w = N_\beta N_\phi$ unique windows.

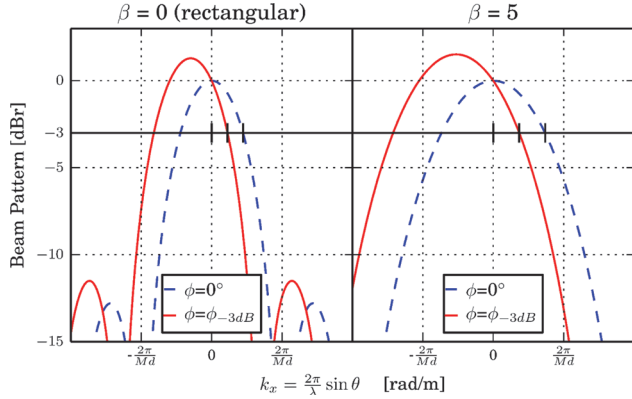


Fig. 1. Each Kaiser window is steered in the interval $\phi \in [0, \phi_{3 \text{ dB}}(\beta)]$. The angle $\phi_{3 \text{ dB}}(\beta)$ is the amount of steering needed for the steered amplitude response to have a -3-dB crossing that is exactly half that of the unsteered window. With each window steered this way we expect the resolution gain to remain predictable and independent of β , and we also effectively constrain the white noise gain of the beamformer.

261 C. Steering Bounds

262 Each window's spatial response is constrained to unit gain in
 263 the look direction. Hence, when it is steered, the white noise
 264 gain must increase and the signal-to-noise ratio must decrease,
 265 as shown in Fig. 1. To limit this, we place an upper bound to
 266 the steering, chosen such that wide windows are allowed to be
 267 steered more than the narrow ones. We call this the upper bound
 268 for steering $\phi_{3 \text{ dB}}(\beta)$, and define it as the steering angle needed
 269 for the steered amplitude response to have a -3-dB crossing
 270 that is exactly half that of the unsteered window. The method
 271 we devised for finding it is described in Appendix A.

272 Henceforth, any steering will be specified relative to this upper
 273 bound. With each window steered this way, we expect the
 274 resolution gain to remain predictable and independent of β , and
 275 we also effectively constrain the white noise gain of the beam-
 276 former.

277 D. Trigonometric Windows

278 While we focus on using LCA with the Kaiser window func-
 279 tion, for comparison, we will also test it with the trigonometric
 280 window function. Its definition is

$$f_m(\alpha) = \alpha - (1 - \alpha) \cos\left(\frac{2\pi m}{M-1}\right) \quad (12)$$

281 where we apply the constraint $\alpha \in [0.5, 1]$ to avoid windows
 282 with negative coefficients. Steering is applied as in (10), and
 283 the α -value that halves the -3-dB distance is found using the
 284 method described in Appendix A.

285 E. Oversampling

286 The ultimate goal of adaptive beamformers is to take the in-
 287 formation available in the wavefield and use it to either improve
 288 image resolution, sidelobe suppression, or preferably both. This
 289 nonlinear processing increases the image bandwidth and intro-
 290 duces a need for a sampling rate higher than the Nyquist rate.

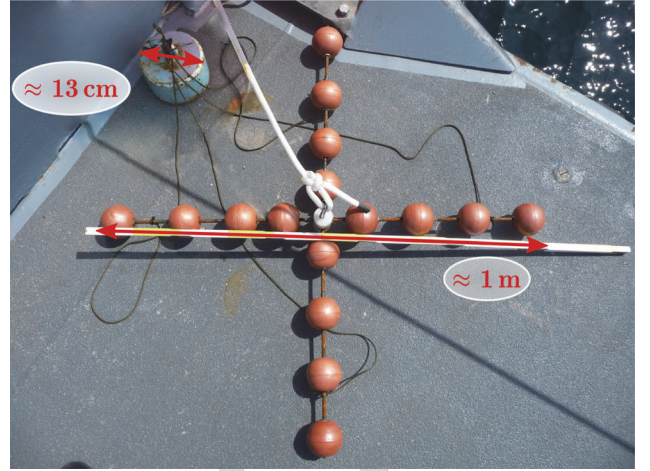


Fig. 2. Submerged object used to test beamforming resolution is a $1 \times 1 \text{ m}^2$ test cross attached to an anchor with a diameter of approximately 13 cm. Source image courtesy of the Bundeswehr Technical Center for Ships and Naval Weapons, Maritime Technology and Research (WTD 71).

For MVDR, a lateral oversampling factor of 10 compared to
 292 the Nyquist rate is often needed to ensure minimal spatial shift
 293 variance in source amplitude [18].

Since LCA operates with the same optimization criterion
 294 as MVDR, we will be using approximately a factor 8 lateral
 295 oversampling for both beamformers. The images appear more
 296 visually pleasing and detailed up to 8. We consider an absolute
 297 minimum to be 2, due to the nonlinear nature of delaying pixels
 298 that are not strictly in the far field, and of displaying the absolute
 299 value of the pixels on a decibel scale. In Media Movie 1,¹
 300 we visualize the effect of changing the lateral oversampling
 301 factor on a set of LCA images. Upon display, the images are all
 302 bilinearly upinterpolated to the same size.

V. RESULTS AND DISCUSSION

To test the performance of the MVDR and LCA beamformers,
 305 we have processed data acquired by the Kongsberg Maritime
 306 autonomous underwater vehicle (AUV) *HUGIN* carrying its 32-
 307 element HISAS1030 sonar [19]. It is a high-resolution sonar
 308 with 1.2-m array length, 100-kHz operating frequency, 30-kHz
 309 bandwidth, and 23° element -3-dB opening angle.
 310

Two different scenes will be studied. One is the 1500 DWT
 311 oil tanker wreck *Holmengraa* lying at a slanted seabed at 77-
 312 m depth outside Horten, Norway [20]. It measures $68 \times 9 \text{ m}^2$
 313 and fills most of the highlighted sector. These data were col-
 314 lected by the Norwegian Defense Research Establishment and
 315 Kongsberg Maritime. The other scene is of a $1 \times 1 \text{ m}^2$ iron res-
 316 olution test cross, connected to an anchor with 13-cm diameter
 317 (Fig. 2). These data were collected by the Bundeswehr Techni-
 318 cal Center for Ships and Naval Weapons, Maritime Technology
 319 and Research (WTD 71).

In the image reconstruction, we have run MVDR with subar-
 320 ray length $L = 16$ and $\epsilon = 1\%$ diagonal loading. Both MVDR
 321

¹See the Supplementary Material that accompanies this paper.

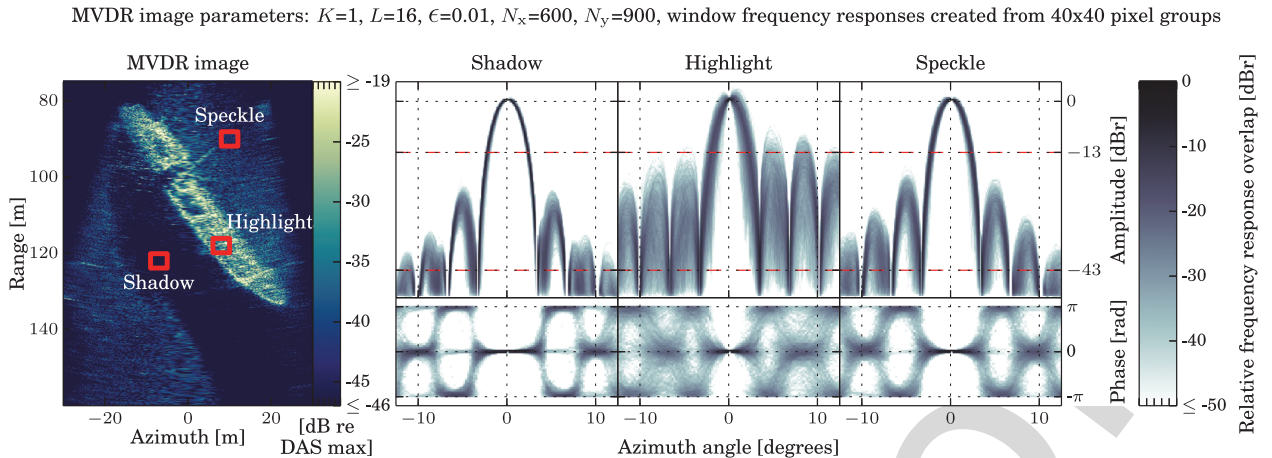


Fig. 3. Determining LCA window type: MVDR image with typical frequency responses for windows used in various pixel regions. (Left) MVDR sectorscan image of the oil tanker Holmengraa, with 40×40 pixel groups for the shadow, highlight, and speckle regions of the image indicated with red boxes. (Right) MVDR window amplitude and phase responses computed from the 40×40 pixel groups. The responses overlay each other and the amount of overlap is colored using a logarithmic scale. The size of the pixel groups was chosen *ad hoc* for the histograms to be visually invariant to a shift in position within the same region. Since each pixel is predelayed into focus, the unsteered responses all have their center at broadside. The dashed red lines at -13 and -43 dB mark the peak sidelobe levels of an unsteered rectangular and the Hamming window, respectively. Note how the responses are more or less symmetric, with very little steering in the shadow region, moderate steering in the speckle region, and steering within roughly 3 dB in the highlight region. The phase varies most in the highlight region where we see the highest contrast.

323 and LCA were run with $K = 1$ temporal averaging. This is a
324 fairly aggressive yet stable set of parameters [15].

325 The results will be presented in the following order: In
326 Section V-A, we discuss typical window responses computed by
327 MVDR, and hypothesize that these can be mimicked by Kaiser
328 windows. In Section V-B, we determine sensible boundaries for
329 the Kaiser parameter β and window steering ϕ . In Section V-C,
330 we discuss how many window variations are needed for LCA to
331 perform well.

332 A. LCA Window Function

333 Assuming that a robust MVDR is the reference method we
334 want LCA to perform similarly to, it seems sensible to create
335 a window database for LCA with spatial responses similar to
336 the ones that MVDR computes. We study this in Fig. 3, where
337 we present the typical amplitude and phase responses for the
338 windows that MVDR creates in shadow, speckle, and highlight
339 regions of the Holmengraa scene.

340 Note in Fig. 3 that MVDR seems to prefer symmetric window
341 responses, even if choosing nonsymmetric ones is free.  Symmetry is most predominant in shadow and speckle regions,
342 while in the highlight region, the windows are approximately
343 symmetric within the illuminated sector of the seafloor. We
344 have observed this symmetry to be a side effect of the averaging
345 steps needed to build the sample covariance matrix, which are
346 required for MVDR to operate with very little to no temporal
347 support in an active system. The peak sidelobe levels of
348 the MVDR windows are mostly between -13 and -43 dB. This
349 corresponds to that of an unsteered rectangular and Hamming
350 window, or an unsteered Kaiser window with $\beta = 0$ and $\beta = 2$,
351 respectively.

352 From this we hypothesize that a good window database LCA
353 can be made using a varied set of Kaiser windows. If they

354 span a suitable range of β -values, and some steering variations
355 are applied to each, we should have responses that resemble
356 those in Fig. 3. The Kaiser window is easy to compute, is fairly
357 insensitive to coefficient inaccuracies, and spans shapes from
358 rectangular to Gaussian. It is also optimal in the sense of having
359 its peak power concentration near the steering angle.
360

361 Unlike the method described by Synnevåg *et al.* [10], we do
362 not let LCA choose from inverted Kaiser windows. These have
363 a mainlobe width narrower than that of the rectangular window,
364 but at the expense of very poor white noise gain. We have found
365 that these windows hardly ever get used on experimental data,
366 in particular steered versions of them. We can infer the same
367 from Fig. 3 by noting that the maximum sidelobe level rarely
368 exceeds the rectangular window level of -13 dB.
369

370 Media Movie 2² animates how Fig. 3 changes as a function
371 of the MVDR subarray length L and temporal averaging K .
372 At $L = 1$, the window responses are rectangular in all areas
373 in the image. At $L = 2$, we observe window responses with
374 slight amplitude variations in the highlight region, but with the
375 phase being 0° in the illuminated seafloor sector. Already at
376 $L = 2$, the MVDR is able to greatly suppress noise. This is a
377 common observation; adding a little flexibility to adapt to the
378 scene has a dramatic effect, but allowing full flexibility is much
379 less significant. The media file also shows that MVDR can be run
380 with subarray sizes $L \in [M/2, 5M/8]$, but only with temporal
381 averaging $K = 1$ or above.

382 B. Kaiser Parameter β and Steering ϕ

383 To determine a suitable range for the Kaiser parameter β
384 and phase steering ϕ , we constructed large and equally sized
385 window databases containing Kaiser windows with varied up-

²See the Supplementary Material that accompanies this paper.

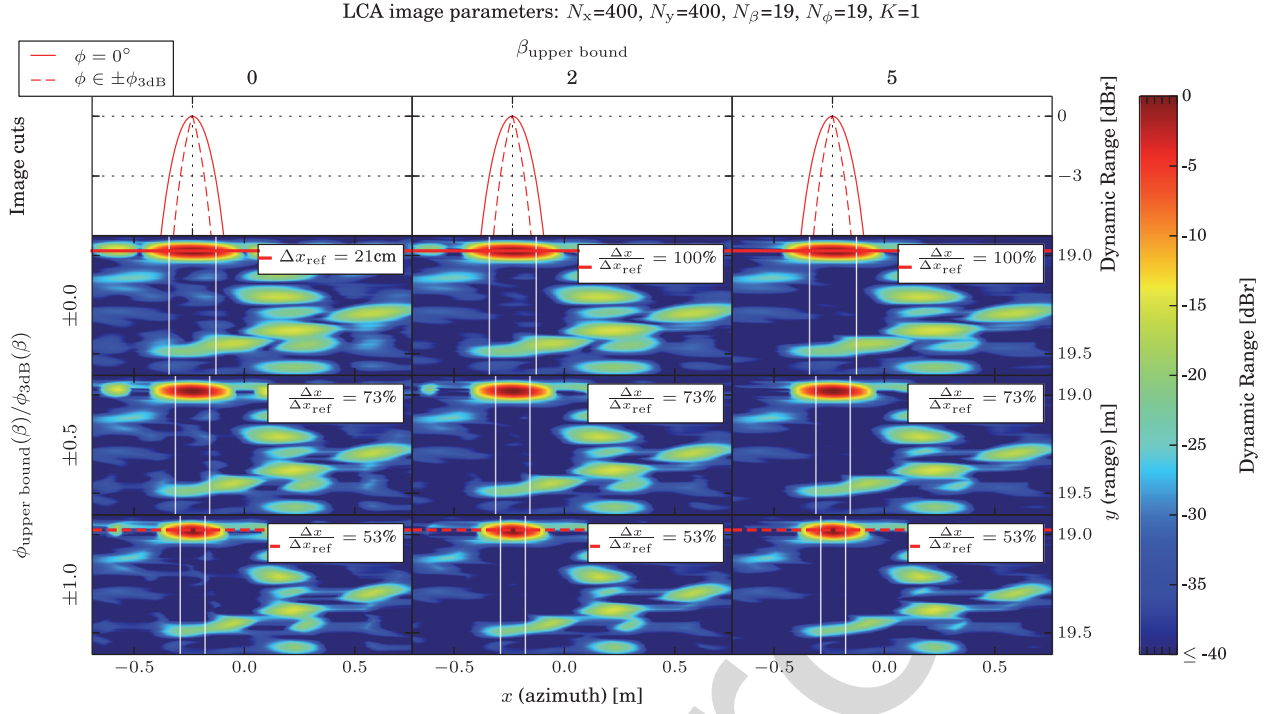


Fig. 4. Determining Kaiser parameter boundaries: LCA images of the resolution test cross and anchor created with a large window database, but where the upper bounds for β and ϕ are varied. The upper left image is equal to DAS with a rectangular window. For all images, we measure the lateral distance Δx between the two -3 -dB points of the anchor (red object). These are specified relatively to the reference distance Δx_{ref} from the upper left DAS image. Upper bound β : Observe that LCA gets better at suppressing sidelobes in the image as we increase the upper bounds for β . Fig. 3 suggests that MVDR prefers windows with sidelobe levels lower than that of Kaiser with $\beta = 2$, but here we observe further improvement going to $\beta = 5$. Upper bound ϕ : As we increase the upper bound of the steering ϕ , we also increase the lateral image resolution.

385 per boundaries for β and ϕ . The lower boundaries were chosen
 386 as $\beta = 0$ and $\phi = 0^\circ$, which includes the rectangularly
 387 weighted DAS image. The resulting images are shown in Fig.
 388 4. In each image, we computed the lateral distance Δx between
 389 the -3 -dB points of the anchor, with the reference Δx_{ref} being
 390 the rectangularly weighted DAS image. A fourth-order poly-
 391 nomial fit was used in this computation. The measure Δx is
 392 also commonly called the full-width half-maximum (FWHM).
 393 In the case of an imaging of a point scatterer, it is closely re-
 394 lated to the resolution of the system. For a rectangular win-
 395 dows, for instance, the system resolution is approximately $\delta x \approx \Delta x / 0.89$ [13].

397 The LCA images in Fig. 4 demonstrate the effect of adjust-
 398 ing the upper bound of β and ϕ . As suggested in Fig. 3, we
 399 first attempt to use $\beta \in [0, 2]$. While this significantly improves
 400 sidelobe suppression, a slight further improvement is observed
 401 up to $\beta \in [0, 5]$. This can likely be explained by the need to com-
 402 pensate for the increased sidelobe levels caused by steering. No
 403 noticeable difference is observed for values higher than $\beta = 5$.
 404 The images also demonstrate that increasing the upper bound for
 405 steering ϕ improves the resolution of the strong scatterers. For
 406 this sonar the Rayleigh resolution is $\delta x \approx 0.0125 \text{ rad} (0.72^\circ)$,
 407 so a point scatterer imaged at 19-m range with a rectangular
 408 DAS will have a lateral $\Delta x \approx 0.0125 \times 19 \text{ m} \times 0.89 = 21 \text{ cm}$.
 409 This is close to the FWHM of the anchor in the DAS image in
 410 Fig. 4, which means that the acoustic fingerprint of the anchor
 411 is similar to a point source. This further implies that the anchor

412 reflections are specular and that we view its rounded side. As we
 413 increase steering to either 50% or 100% of the -3 -dB width, the
 414 FWHM drops to 73% or 53% to that of the rectangular window,
 415 respectively.

416 Fig. 5(a) and (b) illustrates which β and ϕ values LCA prefers
 417 for different regions in the image of the resolution test cross.
 418 Red marker lines are used to pinpoint the cut line, the loca-
 419 tion of the anchor, and strong scatters on the cross. Observe
 420 that in the anchor region only narrow responses ($\beta = 0$) are
 421 used, which is the reason for the anchor FWHM being mea-
 422 sured to the same value regardless of the upper bound of β in
 423 Fig. 4. On other scatterers with strong nearby lateral inter-
 424 ference, LCA prefers wider windows to suppress the interference.
 425 When allowed, LCA prefers to steer windows away from the
 426 sources, but we never let it exceed the $\phi_{3 \text{ dB}}(\beta)$ limit. When
 427 exceeding this bound, we observe oscillation artifacts in the
 428 image.

C. Window Database Size

429 So far we have found it reasonable to use Kaiser win-
 430 dows in the range $\beta \in [0, 5]$, each steered within the range
 431 $|\phi| \in [0, \phi_{3 \text{ dB}}(\beta)]$. What remains is to determine the number
 432 of windows needed. We study this in Fig. 6, where we com-
 433 pare LCA images made from window databases of different
 434 sizes, but with the same parameter boundaries. Included are
 435 the results from using a single window ($N_\beta = 1$) and steering
 436

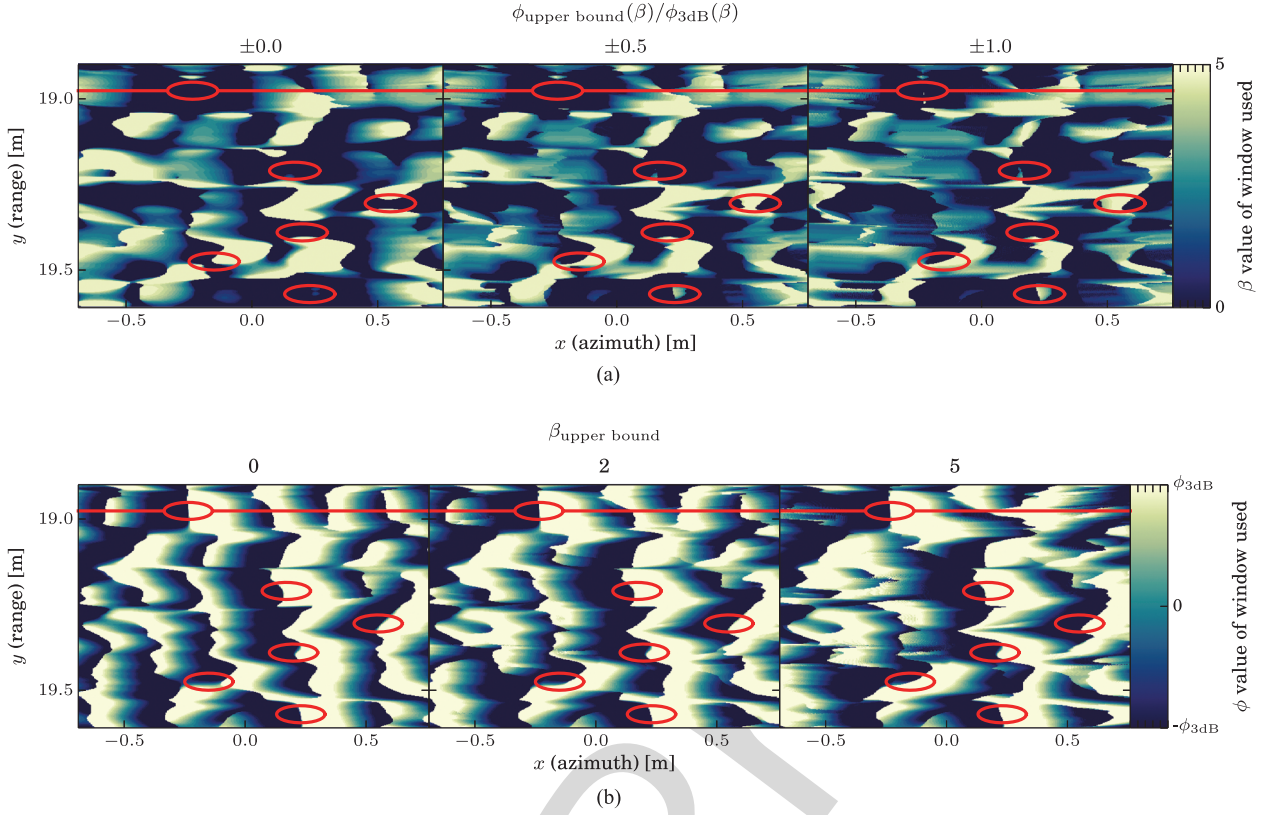


Fig. 5. Kaiser windows chosen for each pixel in the image of the resolution test cross. The underlying image is the one shown in Fig. 4, with the same parameters. Locations of the anchor, the cut line, and the main scatter locations of the cross are marked in red. (a) β -values of the Kaiser window chosen for each image pixel. Note how LCA prefers a narrow response ($\beta = 0$) on the anchor, and on other strong sources with little lateral interference. On the sources where lateral interference is present, it chooses the widest response with the best sidelobe suppression. (b) ϕ -values of the Kaiser window chosen for each image pixel. On strong sources, LCA selects windows that are steered away from the source. This is what improves the FWHM measurement in Fig. 4.

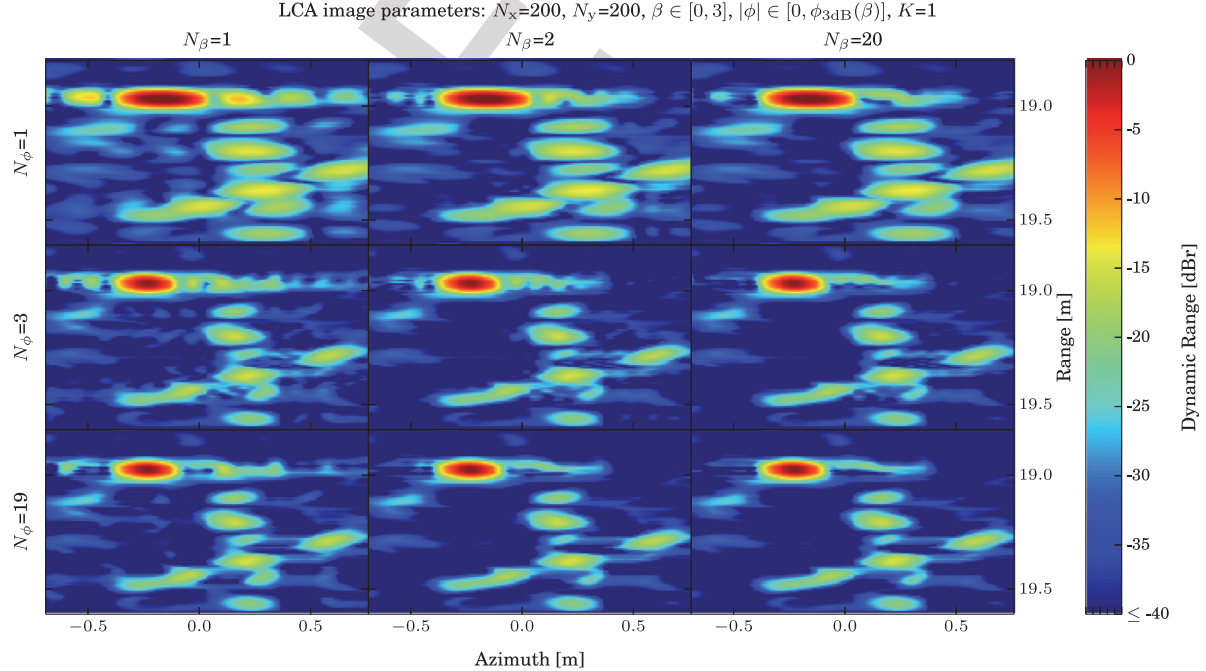


Fig. 6. LCA images using different window database sizes. The window boundaries are the same. The upper left image is identical to a rectangularly weighted DAS. Observe that finer sampling of the β -range improves sidelobe suppression but leaves resolution unchanged. Adding more steering variations improves both sidelobe suppression and resolution. However, using more than $N_\beta = 2$ window types and $N_\phi = 3$ steering angles makes minimal difference.

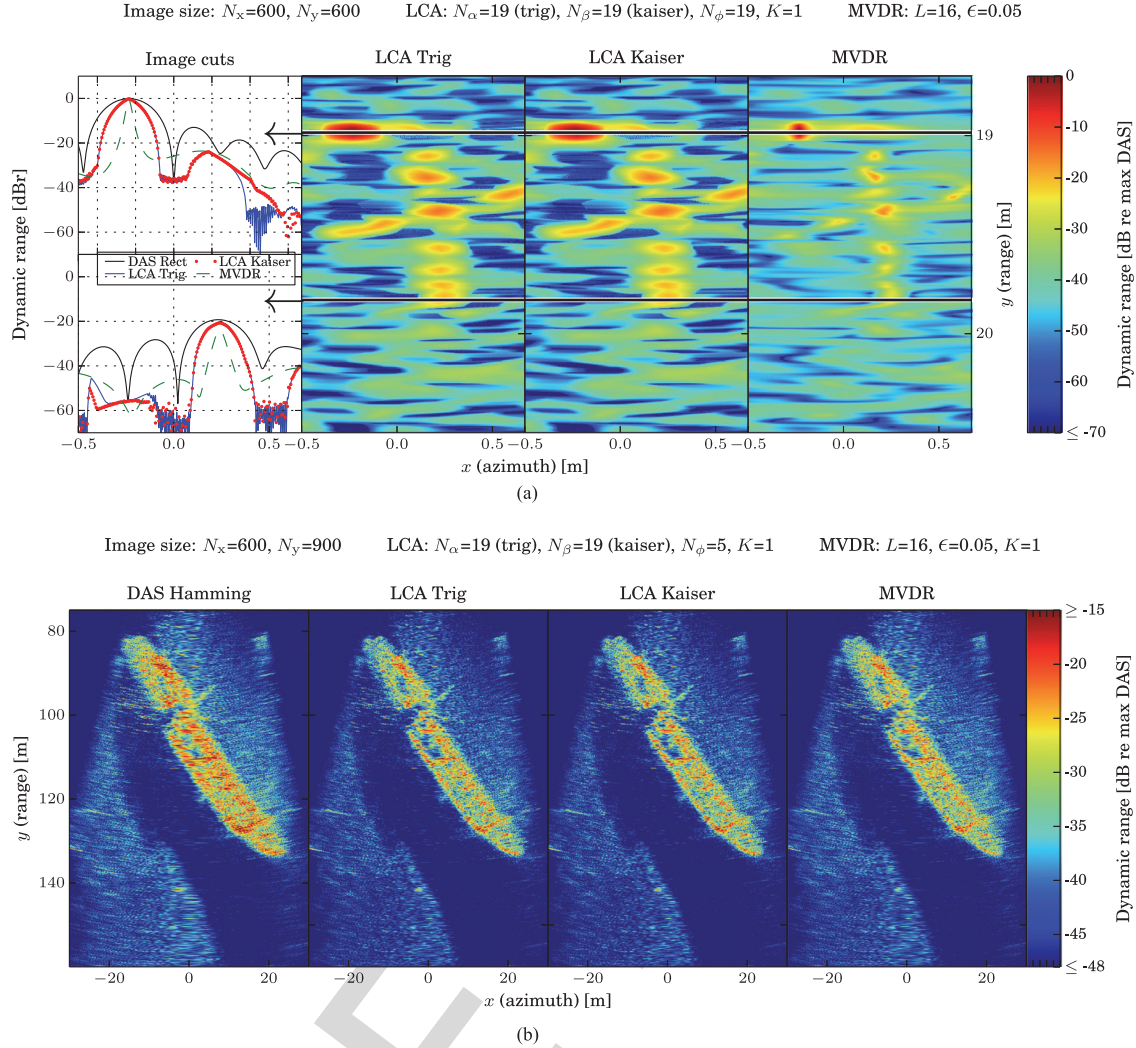


Fig. 7. Comparing image quality of DAS, MVDR, and LCA with Kaiser or trigonometric windows. (a) Image quality of approximate point scatterers found in the resolution test cross scene. Two lateral image cuts are shown in the leftmost figures, along with the response of a rectangularly weighted DAS. Note how the FWHM of LCA sits in between that of DAS and MVDR. Also note how LCA is insensitive to the window type; its performance is near identical whether it uses Kaiser or trigonometric windows. (b) Image quality of the full sector Holmengraa scene. Compared to DAS, the adaptive beamformers produce deeper shadows, sharper edges, and a higher detail level. The adaptive methods produce nearly identical images.

angle ($N_\phi = 1$), which corresponds to an unsteered rectangularly weighted DAS.

Observe that a finer sampling of the β -range improves sidelobe suppression but leaves resolution unchanged. Adding more steering variations improves both sidelobe suppression and resolution. We observe major improvement going to $N_\beta = 2$ and $N_\phi = 3$, but minimal improvement by adding yet more windows.

445 D. Image Quality

446 We compare LCA image quality to that of DAS and MVDR
447 in Fig. 7(a). In Fig. 7(a), we display the images computed by LCA
448 using Kaiser windows, LCA using trigonometric windows, and
449 MVDR. Two lateral image cuts through all images are presented
450 in the left plot. The images and their corresponding cuts are
451 nearly identical for the LCA version with Kaiser windows and
452 the one with trigonometric windows. Compared to DAS, the
453 LCA produces images with an FWHM that lies in between that
454 of DAS and MVDR.

In Fig. 7(b), we show full sector images of the Holmengraa wreck. We compare the images produced by a Hamming weighted DAS, by MVDR and by LCA with Kaiser or trigonometric windows. All the adaptive beamformers produce a sharper and less noisy image than DAS, but the difference between LCA and MVDR is minimal. The LCA image produced with Kaiser windows appears to be identical to that from trigonometric windows.

463 E. Computational Complexity

The computational complexity of MVDR is generally considered to be of $O(M^3)$. However, the implementation we are using is optimized so that building the spatial covariance matrix is of $O(N_k N_L L^2)$, and inverting it is of $O(L^3)$. We describe this implementation in [5] and a beamspace version in [6], where we implement it on a GPU for nearly two orders of magnitude speed increase compared to a straightforward C implementation. However, MVDR is not ideal for GPUs due to the



472 complex data dependencies present in the covariance computation,
 473 and at best we only manage to utilize 10% of the GPUs
 474 maximum theoretical potential.

475 In comparison, LCA is of $O(MN_\beta N_\phi)$, and extremely well
 476 suited for GPUs. Each pixel depends on only a small subset of
 477 data, and the windows can be precomputed and stored in GPU
 478 cache for near-immediate access. Furthermore, if we use the
 479 trigonometric window function, we can solve for the window
 480 parameter analytically, as described in Appendix B. This reduces
 481 the complexity to $O(MN_\phi)$, because the only remaining LCA
 482 parameter to create windows for will be the steering angle.

483 VI. CONCLUSION

484 LCA seeks to improve image resolution and contrast by min-
 485 imizing the power of noise and interference in each image pixel.
 486 This is the same optimization criterion as MVDR uses, but in-
 487 stead of computing an optimal array window like MVDR does,
 488 it selects the best window out of a predefined set. Hence, it can
 489 be viewed as either a reduced and discrete window space ver-
 490 sion of MVDR, or as an advanced multiapodization technique.
 491 In this paper, we have studied which windows we should ideally
 492 let LCA to choose from.

493 We found LCA to be surprisingly insensitive to the exact
 494 window function it is used with, supported by the observation
 495 that near-identical images were produced whether we used the
 496 Kaiser windows or the trigonometric ones. However, LCA must
 497 be able to choose between wide and narrow window responses,
 498 since the wide ones offer the best sidelobe suppression and the
 499 narrow ones offer the best sensitivity. We achieved good results
 500 with two to three Kaiser windows in the range $\beta \in [0, 5]$, and
 501 observed minimal difference when adding more windows or ad-
 502 justing the upper bound of β . For the steering angle, we suggest
 503 a value in the range $\phi \in [\pm\delta\phi_{3\text{dB}}(\beta)]$, where $\phi_{3\text{dB}}(\beta)$ is the
 504 bandwidth of the respective window, and δ is a scaling param-
 505 eter. Setting δ to either 50% or 100% reduces the lateral point
 506 target size to 73% or 53% compared to the rectangular window,
 507 respectively. Hence, this parameter can be used to control the
 508 aggressiveness and resolution gain of LCA.

509 In summary, LCA is an attractive alternative to other adaptive
 510 beamformers due to being very fast, simple to understand, prac-
 511 tically parameter free, inherently robust, and able to produce
 512 images similar to that of MVDR. Contrary to MVDR, it has a
 513 low computational complexity and can be easily and efficiently
 514 accelerated using, for example, GPUs. Also, since LCA per-
 515 forms just as well if we use trigonometric windows instead of
 516 the Kaiser ones, we can compute the optimal window parameter
 517 analytically for any given steering angle and avoid the search
 518 over the window parameter entirely.

519 APPENDIX A STEERING ANGLE

520 One of the goals of this paper was to characterize the win-
 521 dows used by the MVDR method, and then identify a subset of
 522 these that were suitable for use with the LCA method. We de-
 523 termined that the Kaiser function could fit the role of producing
 524 the relevant windows. The spatial response of a steered Kaiser

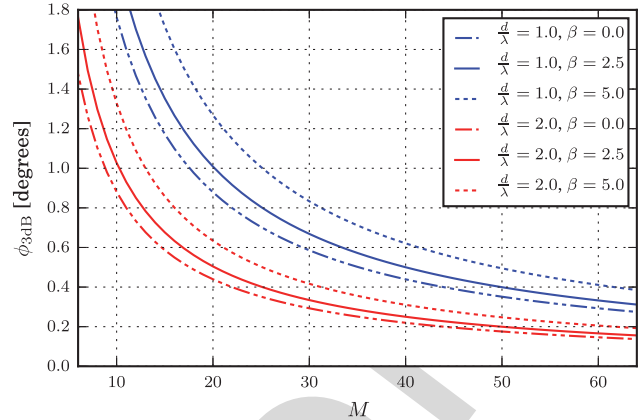


Fig. 8. Steering angle needed to cut the -3-dB distance of the Kaiser window's spatial response in half. The needed amount of steering depends on the number of channels M , the element spacing relative to the wavelength (d/λ) , and the Kaiser parameter β . Note how the angle scales near proportionally with (d/λ) .

window depends on the number of channels M , the element 525
 spacing relative to the wavelength (d/λ) , the Kaiser parameter 526
 β , and the amount of steering ϕ . 527

To control the resolution gain of LCA, we wanted to deter- 528
 mine the extent to which the windows need to be steered to cut 529
 the angle of the -3-dB point of the window's spatial amplitude 530
 response by a fixed amount, say, by a factor 2 as reference. We 531
 computed this steering angle for some common configurations 532
 of the mentioned parameters; see the result in Fig. 8. The bound- 533
 ary values of the Kaiser window are shown, i.e., the rectangular 534
 window at $\beta = 0$ and the near Gaussian window at $\beta = 5$, as 535
 well as the one in between at $\beta = 2.5$. Observe that for a given 536
 M and β , the angle $\phi_{3\text{dB}}$ scales near proportionally with (d/λ) . 537
 We found this to be true also for $(d/\lambda) \in \{0.5, 4\}$. Hence, an 538
 approximate figure for a rather wide range of system parameters 539
 can be derived off this figure. 540

For the sake of completeness, we also supply the source code 541
 (see the Supplementary Material that accompanies this paper). 542

APPENDIX B REDUCING LCA COMPLEXITY

Throughout this paper we have used LCA with the Kaiser 544
 window function. However, as shown in Fig. 7, we can obtain 545
 similar performance using the trigonometric window function. 546
 For this window, we can obtain an analytic solution for the op- 547
 timal value of α in the minimum variance sense. The following 548
 derivation generalizes that of the nonsteered (real) window de- 549
 scribed in, for example, [21] to also apply for the steered (com- 550
 plex) window. We start by inserting the trigonometric function 551
 (12), with applied steering (11), into the beamformer (1) 552

$$\begin{aligned} \mathbf{w}^H \mathbf{x} &= \sum_{m=0}^{M-1} [\mathbf{a}_\phi]_m \left(\alpha - (1-\alpha) \cos \left(\frac{2\pi m}{M-1} \right) \right) x_m^* \\ &= \alpha \mathbf{a}_\phi^T \mathbf{x} - (1-\alpha) \mathbf{b}_\phi^T \mathbf{x} \end{aligned} \quad (13)$$

553 where $[a_\phi]_m$ is the m th component of the steering vector \mathbf{a}_ϕ
 554 defined in (11), and

$$\mathbf{b}_\phi = \text{diag}(\mathbf{a}_\phi) \cdot [1 \cos(\frac{2\pi}{M-1}) \cos(\frac{2\pi 2}{M-1}) \dots 1]^T. \quad (14)$$

555 Unity gain in the look direction is ensured as long as the weights
 556 sum to one

$$\mathbf{w}^T \mathbf{1} = (\alpha \mathbf{a}_\phi - (1 - \alpha) \mathbf{b}_\phi)^T \mathbf{1} = 1. \quad (15)$$

557 This is true for any value of α if $\mathbf{a}_\phi^T \mathbf{1} = 1$ and $\mathbf{b}_\phi^T \mathbf{1} = 1$. Hence,
 558 we preserve the unity gain constraint as long as we normalize
 559 \mathbf{a}_ϕ and \mathbf{b}_ϕ .

560 Now let $a = \mathbf{a}_\phi^T \mathbf{x}$ and $b = \mathbf{b}_\phi^T \mathbf{x}$. The beamformer output can
 561 then be written as

$$\begin{aligned} |\mathbf{w}^H \mathbf{x}|^2 &= |\alpha a - (1 - \alpha) b|^2 \\ &= \alpha^2 (aa^* + ab^* + a^*b + bb^*) \\ &\quad - \alpha (ab^* + a^*b + 2bb^*) + bb^*. \end{aligned} \quad (16)$$

562 This is a convex function with a single minimum, which we find
 563 by differentiating with respect to α and setting equal to 0

$$\begin{aligned} \frac{\partial}{\partial \alpha} |\mathbf{w}^H \mathbf{x}|^2 &= 2\alpha (aa^* + ab^* + a^*b + bb^*) \\ &\quad - (ab^* + a^*b + 2bb^*) = 0 \end{aligned} \quad (17)$$

564 which has the solution

$$\alpha = \frac{ab^* + a^*b + 2bb^*}{2(aa^* + ab^* + a^*b + bb^*)}. \quad (18)$$

565 In this computation, there are only four and seven unique com-
 566 plex additions and multiplications, respectively. If we used this
 567 to analytically solve for α , but perform the search for ϕ , the
 568 computational complexity of LCA would be of $O(MN_\phi)$ in-
 569 stead of $O(MN_\alpha N_\phi)$. The solution for α would also yield the
 570 optimal beamformer output in the minimum variance sense.

ACKNOWLEDGMENT

572 The authors would like to thank Kongsberg Maritime, the
 573 Norwegian Defence Research Establishment (FFI), and Bun-
 574 deswehr Technical Center for Ships and Naval Weapons, Mar-
 575 itime Technology and Research (WTD 71), Germany, for the
 576 equipment and effort needed to acquire data of the resolution
 577 test cross and Holmengraa, as well as for allowing the authors
 578 to use it.

REFERENCES

- 580 [1] J. Capon, "High-resolution frequency-wavenumber spectrum analysis,"
Proc. IEEE, vol. 57, no. 8, pp. 1408–1418, Aug. 1969.
- 581 [2] A. E. A. Blomberg, A. Austeng, R. E. Hansen, and S. A. V. Synnes, "Im-
 583 proving sonar performance in shallow water using adaptive beamforming,"
IEEE J. Ocean. Eng., vol. 38, no. 2, pp. 297–307, Apr. 2013.
- 584 [3] A. E. A. Blomberg, A. Austeng, and R. E. Hansen, "Adaptive beam-
 585 forming applied to a cylindrical sonar array using an interpolated array
 586 transformation," *IEEE J. Ocean. Eng.*, vol. 37, no. 1, pp. 25–34, Jan. 2012.
- 587 [4] K. Lo, "Adaptive array processing for wide-band active sonars," *IEEE
 588 J. Ocean. Eng.*, vol. 29, no. 3, pp. 837–846, Jul. 2004.
- 589 [5] J. I. Buskenes, J. P. Åsen, C.-I. C. Nilsen, and A. Austeng, "An optimized
 591 GPU implementation of the MVDR beamformer for active sonar imaging,"
IEEE J. Ocean. Eng., vol. 40, no. 2, pp. 441–451, Apr. 2015.

- 593 [6] J. P. Åsen, J. I. Buskenes, C.-I. C. Nilsen, A. Austeng, and S. Holm,
 594 "Implementing capon beamforming on a GPU for real-time cardiac ultra-
 595 sound imaging," *IEEE Trans. Ultrason. Ferroelectr. Freq. Control*, vol. 61,
 596 no. 1, pp. 76–85, Jan. 2014.
- 597 [7] K. Kim, S. Park, J. Kim, S.-B. Park, and M. Bae, "A fast minimum
 598 variance beamforming method using principal component analysis," *IEEE
 599 Trans. Ultrason. Ferroelectr. Freq. Control*, vol. 61, no. 6, pp. 930–945,
 600 Jun. 2014.
- 601 [8] B. M. Asl and A. Mahloojifar, "A low-complexity adaptive beam-
 602 former for ultrasound imaging using structured covariance matrix," *IEEE
 603 Trans. Ultrason. Ferroelectr. Freq. Control*, vol. 59, no. 4, pp. 660–667,
 604 Apr. 2012.
- 605 [9] F. Vignon and M. R. Burcher, "Capon beamforming in medical ultrasound
 606 imaging with focused beams," *IEEE Trans. Ultrason. Ferroelectr. Freq.
 607 Control*, vol. 55, no. 3, pp. 619–628, Mar. 2008.
- 608 [10] J.-F. Synnevåg, A. Austeng, and S. Holm, "A low-complexity data-
 609 dependent beamformer," *IEEE Trans. Ultrason. Ferroelectr. Freq. Control*,
 610 vol. 58, no. 2, pp. 281–289, Feb. 2011.
- 611 [11] H. Stankwitz, R. Dallaire, and J. Fienup, "Nonlinear apodization for
 612 sidelobe control in SAR imagery," *IEEE Trans. Aerosp. Electron. Syst.*,
 613 vol. 31, no. 1, pp. 267–279, Jan. 1995.
- 614 [12] J. I. Buskenes, C.-I. C. Nilsen, and A. Austeng, "A low complexity adap-
 615 tive beamformer for active sonar imaging," in *Proc. Underwater Acoust.
 616 Meas., Technol. Results*, 2011. pp. 281–286.
- 617 [13] F. Harris, "On the use of windows for harmonic analysis with the discrete
 618 Fourier transform," *Proc. IEEE*, vol. 66, no. 1, pp. 51–83, Jan. 1978.
- 619 [14] T. Kailath and T.-J. Shan, "Adaptive beamforming for coherent signals
 620 and interference," *IEEE Trans. Acoust. Speech Signal Process.*, vol. 33,
 621 no. 3, pp. 527–536, Jun. 1985.
- 622 [15] J.-F. Synnevåg, A. Austeng, and S. Holm, "Benefits of minimum-variance
 623 beamforming in medical ultrasound imaging," *IEEE Trans. Ultrason. Fer-
 624 roelectr. Freq. Control*, vol. 56, no. 9, pp. 1868–1879, Sep. 2009.
- 625 [16] H. Cox, R. Zeskind, and M. Owen, "Robust adaptive beamforming," *IEEE
 626 Trans. Acoust. Speech Signal Process.*, vol. 35, no. 10, pp. 1365–1376,
 627 Oct. 1987.
- 628 [17] J. N. Maksym, "A robust formulation of an optimum cross-spectral beam-
 629 former for line arrays," *J. Acoust. Soc. Amer.*, vol. 65, no. 4, 1979 Art.
 630 971.
- 631 [18] J. P. Åsen, A. Austeng, and S. Holm, "Capon beamforming and moving
 632 objects—An analysis of lateral shift-invariance," *IEEE Trans. Ultrason.
 633 Ferroelectr. Freq. Control*, vol. 61, no. 7, pp. 1152–1160, Jul. 2014.
- 634 [19] R. E. Hansen, H. J. Callow, T. O. Sabo, and S. A. V. Synnes, "Challenges
 635 in seafloor imaging and mapping with synthetic aperture sonar," *IEEE
 636 Trans. Geosci. Remote Sens.*, vol. 49, no. 10, pp. 3677–3687, Oct. 2011.
- 637 [20] Article of Holmengraa on dykkepedia.com.
- 638 [21] P. Stoica and R. L. Moses, "Nonparametric methods," *Spectral Analysis
 639 of Signals*, Englewood Cliffs, NJ, USA: Prentice-Hall, 2005 2, pp. 23–89.

<http://dykkepedia.com/wiki/Holmengraa> 23. May 2016

Originally copied from wreck database www.skovheim.org
 (run by Nils Erik Skovheim).



Jo Inge Buskenes received the B.Sc. degree in electrical engineering from Gjøvik College University, Gjøvik, Norway, in 2007 and the M.Sc. degree in instrumentation for particle physics from the University of Oslo, Oslo, Norway, in 2010, where he is currently working toward the Ph.D. degree in acoustic image reconstruction and high performance computing.

His industry experience includes development of digital electronics at the European Organization for Nuclear Research (CERN), Geneva, Switzerland (2007–2008). He has lectured in digital signal processing at the Gjøvik College University (2009) and at the University of Oslo (2010–2013). Current affiliation is with The Norwegian Defence Research Establishment, Kjeller, Norway, for which he is developing radar systems (2015–), and formerly sonar systems (2009, 2013). His research interests include radar and sonar technology, adaptive image reconstruction, high-performance computing, intelligent detector design, and open-source software.

658
659
660
661
662
663
664
665
666
667
668
669
670
671
672



Roy Edgar Hansen (M'07) received the M.Sc. and Ph.D. degrees in physics from the University of Tromsø, Tromsø, Norway, in 1992 and 1999, respectively.

From 1992 to 2000, he was with the Norwegian research company TRIAD, working on multistatic sonar, multistatic radar, synthetic aperture radar (SAR), and underwater communications. Since 2000, he has been with the Norwegian Defence Research Establishment (FFI), Kjeller, Norway. He is currently Principal Scientist and team leader for the autonomous underwater vehicle development and the synthetic aperture sonar development at FFI. He is also Adjunct Associated Professor at the University of Oslo, Oslo, Norway.



Andreas Austeng was born in Oslo, Norway, in 1970. He received the M.Sc. degree in physics and the Ph.D. degree in computer science from the University of Oslo, Oslo, Norway, in 1996 and 2001, respectively.

Since 2001, he has been with the Department of Informatics, University of Oslo, first as a Postdoctoral Research Fellow and currently as an Associate Professor. His research interests include signal and array processing for acoustical imaging.

673
674
675
676
677
678
679
680
681
682

IEEE Proof

QUERIES

- 684 Q1. Author: Please supply index terms/keywords for your paper. To download the IEEE Taxonomy go to
685 http://www.ieee.org/documents/taxonomy_v101.pdf
- 686 Q2. Author: Please specify section.
- 687 Q3. Author: Please provide page range or DOI in [12].
- 688 Q4. Author: Please provide complete information in [20]: url, date, author.

IEEE Proof